a reprint from Applied Optics

Infrared transmission through cirrus clouds: a radiative model for target detection

K. N. Liou, Y. Takano, S. C. Ou, A. Heymsfield, and W. Kreiss

An IR transmission model for thin and subvisual cirrus clouds composed of hexagonal ice crystals with a specific use for target detection has been developed. The present model includes parameterizations of the ice crystal size distribution and the position of cirrus clouds in terms of ambient temperature. To facilitate the scattering and absorption calculations for hexagonal column and plate crystals in connection with transmission calculations, we have developed parameterized equations for their single scattering properties by using the results computed from a geometric ray-tracing program. The successive order-of-scattering approach has been used to account for multiple scattering of ice crystals associated with a target–detector system. The direct radiance, path radiance, and radiances produced by multiple scattering and background radiation involving cirrus clouds have been computed for 3.7- and 10-μm wavelengths. We show that the background radiance at the 3.7-μm wavelength is relatively small so that a high contrast may be obtained using this wavelength for the detection of airborne and ground-based objects in the presence of thin cirrus clouds. Finally, using the present model, including a simple prediction scheme for the ice crystal size distribution and cloud position, the transmission of infrared radiation through cirrus clouds can be efficiently evaluated if the target–detector geometry is defined.

I. Introduction

It has been recognized that cirrus clouds are global in nature, relatively stable and long-lived, and generally reside in the upper troposphere and lower stratosphere. They are mostly associated with large scale weather disturbances and deep cumulus outflows.[1] From *in situ* aircraft observations, it has been determined that cirrus clouds are largely composed of nonspherical columns, plates, and bullet rosettes.[2] Because of low ice crystal concentrations and their high location in the atmosphere, cirrus clouds are normally semitransparent and nonblack. For this reason, there are significant problems in the development of satellite remote sensing techniques for the mapping of cirrus clouds over the globe. As pointed out in Liou,[1] some thin cirrus clouds may be undetected by satellite visible and IR channels and/or ground observers.

Owing to their high location in the atmosphere, thin and subvisual cirrus clouds could have a significant effect on the passive detection of IR signatures from high flying aircraft and hot ground sources. Significant attenuation may occur from long path transmission when thin cirrus clouds are present. In order to quantitatively assess the IR transmission through cirrus clouds, it is necessary to develop a model that accounts for the effects of the nonsphericity of ice crystals and multiple scattering involving these particles. The objective of this paper is to develop an IR transmission model for cirrus clouds, using the basic scattering and absorption data for hexagonal ice crystals. In Sec. II we present parameterization equations for the ice crystal size distribution in terms of temperature based on size spectra measured from aircraft. In addition, the single-scattering properties of hexagonal ice crystals are also parameterized using the data computed from the light scattering program developed by Takano and Liou.[3] The formulation of IR transmission through cirrus clouds for a target–detector system is given in Sec. III. Computational results, using 3.7- and 10-μm wavelengths, are described in Sec. IV. Finally, conclusions are given in Sec. V.

II. Parameterization of Cirrus Microphysical and Single-Scattering Properties

To facilitate the computation of light scattering by nonspherical ice crystals for applications to the trans-

W. Kreiss is with Horizons Technology, Inc. 3990 Ruffin Road, San Diego, California 92123; A. Heymsfield is with National Center for Amospheric Research, Boulder, Colorado 80303; the other authors are with University of Utah, Meteorology Department, Center for Atmospheric & Remote Sounding Studies, Salt Lake City, Utah 84112.

Received 26 June 1989.
0003-6935/90/131886-11$02.00/0.

mission problems associated with cirrus clouds, we wish to develop parameterization equations for the ice crystal size distribution as a function of temperature and for the scattering and absorption properties of hexagonal ice crystals.

A series of *in situ* measurements of the microphysical properties of cirrus clouds associated with warm frontal overrunning systems, warm frontal occlusions, closed lows aloft, and the jet stream in midlatitudes have been undertaken by Heymsfield.[4,5] There is strong evidence from the data that the maximum dimension of ice crystals and ice water content are correlated with temperature. Heymsfield and Platt[2] grouped the observed data for the ice crystal concentration as a function of maximum dimension and temperature for a 5°C interval from −20 to −60°C. Based on this grouping, the ice crystal size distribution in cirrus clouds can be represented by two equations in the forms

$$n(D) = \begin{cases} A_1 \times D^{B_1} \times \text{IWC} & \text{for } D \le D_0, \quad (1a) \\ A_2 \times D^{B_2} \times \text{IWC} & \text{for } D > D_0, \quad (1b) \end{cases}$$

where n is in units of $\text{m}^{-3}\,\mu\text{m}^{-1}$, D the crystal maximum dimension in μm, IWC the ice water content in g m^{-3}, B_1 and B_2 the slopes of the curves, A_1 and A_2 the coefficients related to ice crystal concentrations at 100 and 1000 μm, respectively, and the crystal maximum dimension criterion is given by

$$D_0 = \left(\frac{A_2}{A_1}\right)^{1/(B_1 - B_2)}. \quad (2)$$

The values of A_1, A_2, B_1, B_2, and IWC are related to temperatures in the range of −20 to −60°C. Once the temperature is given, the ice crystal size distribution may be inferred from Eqs. (1) and (2). The smallest D measured from the aircraft experiment and presented by Heymsfield is 20 μm, and the resulting ice crystal size distributions are for cirrus clouds in midlatitudes.

The extinction cross section C_e for randomly oriented hexagonal ice crystals of the same size can be expressed by[3]

$$C_e = \frac{3}{2}(w/2)^2(\sqrt{3} + 4D/w), \quad (3)$$

where w is the width of the basal plane of a hexagonal ice crystal and D the maximum dimension defined previously. When absorption is small, the absorption cross section C_a is proportional to the product of the absorption coefficient k_i and volume V, where $k_i = 4\pi m_i/\lambda$, m_i is the imaginary part of the complex refractive index, λ is the wavelength, and $V = 3\sqrt{3}\,w^2D/8$ for a hexagonal cylinder. The single-scattering albedo is defined as the ratio of the scattering cross section C_s to the extinction cross section in the form

$$\tilde{\omega} = \frac{C_s}{C_e} = 1 - \frac{C_a}{C_e}. \quad (4)$$

Thus for weak absorption, $(1 - \tilde{\omega})$, the single-scattering coalbedo, must be proportional to a physical parameter defined by

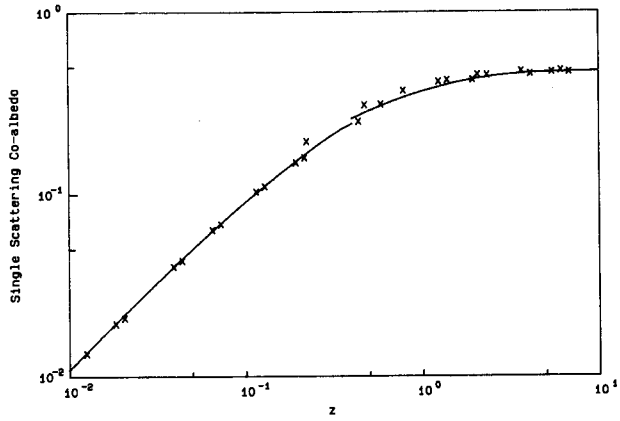

Fig. 1. Computed single-scattering coalbedo, $1 - \tilde{\omega}$, denoted by crosses and the fitted curve as a function of the physical parameter z defined in Eq. (5). There is a slight discontinuity at $z = 0.4$ that defines strong and weak absorption.

$$z = k_i(w/2)\frac{3\sqrt{3}(D/w)}{\sqrt{3} + 4(D/w)}. \quad (5)$$

Based on numerical calculations involving a number of wavelengths, particle sizes w, and aspect ratios D/w, we find that the single-scattering albedo can be parameterized in terms of a fourth order polynomial in the form

$$\tilde{\omega} = 1 - \sum_{n=1}^{4} f_n z^n \quad \text{for} \quad z < 0.4, \quad (6)$$

where $f_1 = 1.1128$, $f_2 = -2.5576$, $f_3 = 5.6257$, and $f_4 = -5.9498$. For weak absorption, the lowest single-scattering albdo $\tilde{\omega} = 0.7564$, corresponds to $z = 0.4$. Eq. (6) fits the exact values of $\tilde{\omega}$ within 3%. In the computation, the complex refractive indices, $m(= m_r - im_i)$, for ice were taken from Warren.[6]

For strong absorption, the scattering cross section is related to Fraunhofer diffraction and external reflections. Rays undergo refractions and internal reflections are largely absorbed and contribute little to scattering. In the limit of geometric optics, the scattering cross section due to Fraunhofer diffraction is one-half of the extraction cross section. The scattered energy per unit incident energy due to the contribution of external reflections for randomly oriented ice crystals of the same size is ~0.06. Using an extinction efficiency of 2, the single-scattering albedo in the limit of geometric optics is (1 + 0.06)/2 = 0.53. Consistent with the physical parameter defined in Eq. (5), we find the following parameterization fits the computed single-scattering albedo:

$$\tilde{\omega} = 1 - 0.47[1 - \exp(az^b)], \qquad z \ge 0.4, \quad (7)$$

where $a = -1.5051$ and $b = 0.6789$. When $z \to \infty$, i.e., in the geometric optics limit, we have $\tilde{\omega} = 0.53$ in agreement with the preceding analysis. The parameterized equation gives an accuracy of better than 3%. Figure 1 shows the single-scattering coalbedo as a function of the physical parameter z in the range from 0.01 to 10. The crosses are the exact values computed

from the light scattering program, while the solid curves are the best fits to data points. There is a slight discontinuity at $z = 0.4$ that defines weak and strong absorption because of the different mathematical functions used in the fittings.

Equations (3), (6) and (7) were derived for ice crystal size in terms of the maximum dimension and width. The width of a hexagonal ice crystal can be related to the maximum dimension on the basis of *in situ* ice crystal size observations.[7] The ice crystal size distribution given in Eq. (1) defines both the size and shape (in terms of the aspect ratio D/w) of ice crystals. The scattering and extinction cross sections for a sample of ice crystals with sizes defined by Eq. (1) can be obtained by performing an integration over this size distribution function. The averaged extinction cross section $\hat{C}_e$ is defined by

$$\hat{C}_e = \frac{1}{N}\int_0^\infty C_e(D)n(D)dD, \tag{8}$$

where the total number density

$$N = \int_0^\infty n(D)dD. \tag{9}$$

The average scattering cross-section $\hat{C}_s$ is given by

$$\hat{C}_s(\lambda) = \frac{1}{N}\int_0^\infty \tilde{\omega}(D,\lambda)C_e(D)n(D)dD. \tag{10}$$

The extinction, scattering, and absorption coefficients, per unit length, can be obtained, respectively, from

$$\left.\begin{aligned}\beta_e(\lambda) &= N\hat{C}_e(\lambda)\\ \beta_s(\lambda) &= N\hat{C}_s(\lambda)\\ \beta_a(\lambda) &= \beta_e(\lambda) - \beta_s(\lambda)\end{aligned}\right\}. \tag{11}$$

The preceding extinction coefficient and single-scattering albedo parameterizations can be applied to any imaginary refractive index, size parameter, and aspect ratio. For the calculation of the phase function, the exact light scattering program must be used. However, the phase function does not vary significantly with wavelength when compared with the single-scattering albedo. For this reason we may use a limited number of representative wavelengths and ice crystal size distributions for phase function computations.

Recently, Platt and Harshvardhan[8] have derived a parameterized equation for the absorption coefficient of cirrus clouds in terms of temperature, based on a large number of measurement data obtained from the ground-based lidar and passive radiometer located at 38 and 12.4°S latitudes. They found that averaging over many cases (typically 400 observations), the cirrus IR absorption coefficient is a well defined monotonic function of temperature within a temperature range from −77 to −5°C. A direct comparison of the present parameterization for the single-scattering properties of cirrus clouds with their results appears not to be entirely appropriate because there were no concurrent observations of ice crystal size distributions during the ground-based experiments. However, to have a general comparison, we computed the absorption coefficient from the preceding parameterized equations at the 11-μm wavelength and obtained values of 0.41, 0.30, and 0.07 km^{-1} for temperatures of −25, −35, and −45°C, respectively. The results of Platt and Harshvardhan for the same temperatures are ~0.52, 0.36, and 0.22, which are in the range of the present values that are valid for cirrus clouds in midlatitudes. The differences in the absorption coefficient for colder temperatures are probably due to different ice crystal size distributions involved and the possibility of small ice crystals in tropical cirrus that were not accounted for in the present treatment.

III. Formulation of IR Transmission through Cirrus Clouds

In this section we present basic formulations concerning the IR transmission through cirrus clouds with a specific application to a target-detector system. We first consider the basic radiative transfer equation for diffuse radiance I in the form

$$-\frac{dI(s,\Omega)}{\beta_e ds} = I(s,\Omega) - J(s,\Omega), \tag{12}$$

where the source function is defined by

$$J(s,\Omega) = \frac{\tilde{\omega}}{4\pi}\int_{4\pi} I(s,\Omega')P(\Omega',\Omega)d\Omega' + (1-\tilde{\omega})B(T). \tag{13}$$

In these equations, s denotes the path length along the radiation stream, P the scattering phase function which is a function of the incoming and outgoing solid angles, Ω' and Ω, respectively, and B the Planck function for a temperature, T. Other notations have been defined previously. The differential solid angle $d\Omega = d\mu d\phi$, with $\mu = \cos\theta$, θ the zenith angle, and ϕ the azimuthal angle.

From Eq. (12), the formal solution for diffuse radiation at position $s = 0$ is given by

$$I(0,\Omega) = I(s,\Omega)\exp(-\beta_e s) + \int_0^s J(s',\Omega)\exp(-\beta_e s')\beta_e ds'. \tag{14}$$

The first term on the right-hand side of Eq. (14) represents the direct transmission, while the second is related to multiple scattering contributions. To apply the preceding IR radiative transfer equations to a target–detector system, we must consider the contributions of emitted and scattered radiation that the detector would receive within its field-of-view. There are four radiation sources: direct transmission of the emitted energy from the target, multiple scattering of the emitted energy by cloud particles, background radiance, and path radiance. The details of these sources are described below.

A. Direct Transmission

As shown in Fig. 2(a), the solid angle with respect to the target that is viewed from the detector is

$$\Delta\Omega_t = \pi r_t^2/s^2, \tag{15}$$

where r_t is the effective radius of the target, and the

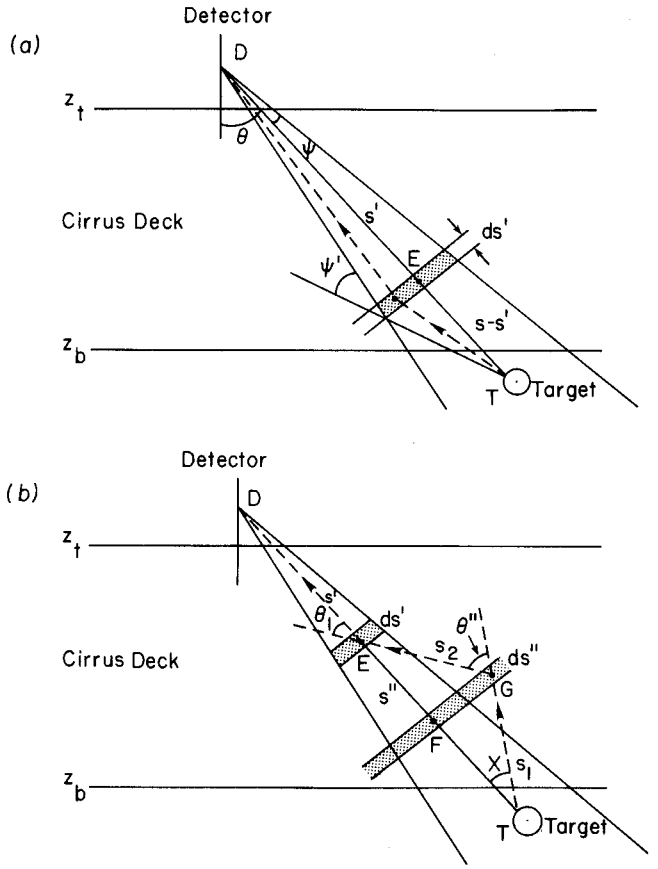

Fig. 2. (a) First-order scattering contribution and definitions of the nadir angle, θ, half beamwidth of the detector ψ, and path length s, in a target–detector system. In this diagram, $s' = DE$, and $s - s' = ET$. (b) Contribution of order of scattering higher than the first in a target–detector system. In this diagram, $s' = DE$, $s'' = EF$, $s_1 = TG$, and $s_2 = GE$. Other notations are defined in the text.

path length $s = \Delta z/\mu$, i.e., the distance between the target and the detector, where Δz is the thickness of the cloud and μ the cosine of the zenith angle of the detector. The solid angle associated with the detector field-of-view is

$$\Delta\Omega = \pi\psi^2, \tag{16}$$

where ψ is the half beamwidth of the detector.

The target with an effective temperature T_t emits radiation in all directions and a part of this radiation is transmitted to the position of the detector. Taking into account the relative solid angles with respect to the target and detector, the direct transmitted radiance may be expressed by

$$I_d(0,\Omega) = \left(\frac{r_t}{s\psi}\right)^2 B(T_t)\exp(-\beta_e s). \tag{17}$$

For IR emission, the transfer of radiation is independent of the azimuthal angle.

B. First-Order Scattering Contribution

We shall approach the multiple scattering problem by using the order-of-scattering method. Based on the solution given in Eq. (14), we may write

$$I^{(n)}(0,\Omega) = \int_0^s J^{(n)}(s',\Omega)\exp(-\beta_e s')\beta_e ds', \qquad n = 1,2,\ldots \tag{18}$$

Here, $n = 1$ denotes the first-order scattering, $n = 2$ the second-order scattering, and so on. The source function in this case is associated with scattering only. Thus from the source function defined in Eq. (13), we have

$$J^{(n)}(s',\Omega) = \frac{\tilde{\omega}}{4\pi}\int_{\Delta\Omega} I^{(n-1)}(s',\Omega')P(\Omega',\Omega)d\Omega'. \tag{19}$$

Equations (18) and (19) can be used to generate high-order multiple scattering contributions iteratively. This is referred to as the order-of-scattering method in radiative transfer. From Eq. (17) for the direct transmitted radiance, the radiance for the zero-order scattering may be written

$$I^{(0)}(s',\Omega) = \left(\frac{r_t}{s\psi}\right)^2 B(T_t)\exp[-\beta_e(s - s')], \tag{20}$$

where s' is defined in Fig. 2(a). From Eq. (19) the source function asociated with the first-order scattering is given by

$$J^{(1)}(s',\Omega) = \frac{\tilde{\omega}}{4\pi} I^{(0)}(s',\Omega)\int_{\Delta\Omega^{(1)}} P(\Omega',\Omega)d\Omega'. \tag{21}$$

The solid angle under which the detector can receive the scattered radiation is

$$\Delta\Omega^{(1)} = 2\pi\psi'. \tag{22}$$

From the geometry illustrated in Fig. 2(a), the angular limit for the zenith angle may be expressed by

$$\psi' = \psi + \tan^{-1}[s'\tan\psi/(s - s')]. \tag{23}$$

The scattered radiance at position $s = 0$ due to the first-order scattering is then

$$I^{(1)}(0,\Omega) = \int_0^s J^{(1)}(s',\Omega)\exp(-\beta_e s')\beta_e ds'. \tag{24}$$

C. Contribution from Scattering More Than Once

In reference to the geometry shown in Fig. 2(b), contributions to the received energy may come from the scattering of cloud particles outside of the detector field-of-view. In this case, scattering must occur more than once. The radiance associated with the zero-order scattering may be written

$$I^{(0)}(s') = \left(\frac{r_t}{s\psi}\right)^2 B(T_t)\exp(-\beta_e s_1), \tag{25}$$

where s_1 is the path length defined in Fig. 2(b). It is given by

$$s_1 = (s - s'')/\cos X. \tag{26}$$

From the geometry, the angle X is related to the path lengths s, s', and s'', and the scattering angle Θ'' in the form

$$\tan X = \frac{-(s - s'') + [(s - s')^2 + 4(s - s'')(s'' - s')\tan^2\Theta'']^{1/2}}{2(s - s')\tan\Theta''}. \tag{27}$$

Following the same procedures as described in the preceding section, the source function associated with the first-order scattering is as follows:

$$J^{(1)}(s',\Omega'') = \frac{\tilde{\omega}}{4\pi} I^{(0)}(s') \int_{\Delta\Omega^{(1)\to(2)}} P(\Omega',\Omega'')d\Omega', \tag{28}$$

where the solid angle is given by

$$\Delta\Omega^{(1)\to(2)} = 2\pi(\psi_2 - \psi_1), \tag{29}$$

with

$$\psi_1 = 0, \psi_2 = \min(\xi_1,\xi_2) \text{ for } s'' > s', \tag{30}$$

$$\psi_1 = \max(\xi_1,\xi_2), \psi_2 = \pi \text{ for } s'' < s', \tag{31}$$

$$\xi_1 = \pi - \theta + \tan^{-1}[(s - s'')/(s' - s'') \cot\theta], \tag{32}$$

$$\xi_2 = \pi - \tan^{-1}[(s - s'')/s'' \cot\theta] + \tan^{-1}[(s' - s'')/s'' \cot\theta], \tag{33}$$

$$\theta = \cos^{-1}\mu. \tag{34}$$

We may express the scattered radiance at position $s = s'$ due to the first-order scattering in the form

$$I^{(1)}(s',\Omega') = \int_0^s J^{(1)}(s',\Omega') \exp(-\beta_e s_2)\beta_e ds''. \tag{35}$$

The path length, s_2, for attenuation may be expressed by

$$s_2 = (s'' - s')/\cos\Theta_1, \tag{36}$$

where

$$\Theta_1 = \Theta'' - X, \tag{37}$$

with Θ'' the scattering angle and the angle X is defined in Eq. (27).

The source function associated with the second-order scattering may be written

$$J^{(2)}(s',\Omega) = \frac{\tilde{\omega}}{4\pi} \int_{\Delta\Omega^{(2)}} I^{(1)}(s',\Omega'')P(\Omega'',\Omega)d\Omega''. \tag{38}$$

From Fig. 2(b), the appropriate solid angle in this case is given by

$$\Delta\Omega^{(2)} = 2\pi[(\Theta_1 + \psi) - (\Theta_1 - \psi)], \tag{39}$$

where ψ is the half angle of the detector defined previously, and Θ_1 is defined in Eq. (37). The radiance for the second-order scattering that can be detected at position $s = 0$ may then be written

$$I^{(2)}(0,\Omega) = \int_0^s J^{(2)}(s',\Omega) \exp(-\beta_e s')\beta_e ds'. \tag{40}$$

The geometry for scattering more than twice is the same as that for the second-order scattering. Thus we may generalize the formulation for the second-order scattering to n-th-order scattering and write

$$J^{(n)}(s',\Omega) = \frac{\tilde{\omega}}{4\pi} \int_{\Delta\Omega^{(n)}} I^{(n-1)}(s',\Omega'')P(\Omega'',\Omega)d\Omega'', \tag{41}$$

$$I^{(n)}(0,\Omega) = \int_0^s J^{(n)}(s',\Omega) \exp(-\beta_e s')\beta_e ds', n \geq 3, \tag{42}$$

where $\Delta\Omega^{(n)} = \Delta\Omega^{(2)}$.

Combining the contributions from the direct transmission, first-order scattering, and multiple scattering, the total radiance that can be detected within the detector field-of-view may be expressed by

$$I_t(0,\Omega) = I_d(0,\Omega) + \sum_{n=1}^{N} I^{(n)}(0,\Omega), \tag{43}$$

where N denotes the total number of scattering events. We define a modified extinction coefficient β_e^* which takes into account the multiple scattering effect such that

$$I_t(0,\Omega) \cong \left(\frac{r_t}{s\psi}\right)^2 B(T_t) \exp(-\beta_e^* s). \tag{44}$$

Thus we have

$$\frac{I_t(0,\Omega)}{I_d(0,\Omega)} = \exp[-\beta_e s(k - 1)], \tag{45}$$

where

$$k = \beta_e^*/\beta_e \leq 1. \tag{46}$$

The factor k is a parameter that accounts for the multiple scattering contribution.

D. Background Radiance, Path Radiance, and Contrast

In addition to the contribution from the direct transmission from a target and multiple scattering of cloud particles, background and path radiances should also be considered. The background radiance I_b is the radiance that is produced by the cloud–atmosphere–surface system at the cloud top where the detector is located. This radiance can be computed from the radiative transfer program for the cloud–atmosphere–surface system developed by Takano and Liou.[9]

The path radiance is the radiance arising from the multiple scattering of cloud particles between the cloud top and bottom. Referring to Eq. (14), it is defined by

$$I_p(0,\Omega) = \int_0^s J(s',\Omega) \exp(-\beta_e s')\beta_e ds'. \tag{47}$$

The background radiance is partially blocked by the target with respect to the detector. Thus the radiance received by the detector due to the contribution of the background is proportional to $[1 - (r_t/s\psi)^2]$. Including the background radiance, path radiance, and radiances produced by the direct transmission and multiple scattering of cloud particles, the total radiance observed by the detector is given by

$$I_0 = [1 - (r_t/s\psi)^2]I_b + (r_t/s\psi)^2 I_p + I_t, \tag{48}$$

where I_t is defined in Eq. (43). Finally, using the preceding definitions, the contrast is defined by

$$C = (I_0 - I_b)/I_b. \tag{49}$$

The contrast of a target against the background depends significantly on the geometric factor $(r_t/s\psi)$, and the target temperature contained in Eq. (44).

IV. Computational Results

In Sec. II, we illustrate that the ice crystal size distribution may be parameterized in terms of temperature, and that the single-scattering properties of ice crystals for any given wavelength may be efficiently computed by using parameterized equations. For applications

to IR transmission through cirrus clouds, the position of their heights must be known. The prediction of cloud heights requires a model for the cloud formation, which could be extremely involved. For cirrus clouds, such a model has not been available up to now. We shall present a simple empirical expression, which could be of some use in relating the cirrus cloud height with the relative humidity (RH).

The supersaturation with respect to ice S_i is a function of temperature and RH, which is defined as the ratio of the ambient vapor pressure e to the saturation vapor pressure over water e_s. If we let the saturation vapor pressure over ice be denoted as e_i, from the definitions of e_i and e_s, we have

$$\mathrm{RH} = \frac{e}{e_i}\left(\frac{e_i}{e_s}\right) = (1 + S_i)\exp\left[\frac{1}{R_v}\left(\frac{1}{T_o} - \frac{1}{T}\right)(L_s - L)\right], \quad (50)$$

where R_v is the gas constant for water vapor, T_o the freezing temperature in kelvins, and L_s and L the latent heat for the phase transitions between vapor and ice, and vapor and water, respectively. The exponential function can be fitted by $\exp[c(T\text{-}273)]$, where $c = 9.24 \times 10^{-3}$, with an accuracy within a few percent over the temperature range 0 to −60°C. From measurements with rawinsondes, RHs have been found to be usually biased downward by ~10% at the temperatures where ice clouds are present.[10] To err on the conservative side we set a threshold RH upon which an ice crystal cloud may be generated by

$$\mathrm{RH}_c \simeq 0.9\exp[c(T\text{-}273)]. \quad (51)$$

In this manner, the threshold RH is expressed in terms of temperature. This equation does not consider evaporative regions located below the ice growth layer. If the ambient RH > RH_c cirrus clouds are present in the atmosphere. This expression has been used to relate the observed RH and cirrus cloud height and gives a height accuracy within ~0.5 km for a number of observational data (Heymsfield, unpublished data). We realize that the prediction of the position of cirrus clouds using the RH technique is primitive and requires further verification. Nevertheless, the preceding parameterization offers a simple and efficient means of producing cirrus clouds. This is sufficient as a first approximation for the formulation of IR transmission through cirrus clouds.

On the basis of the preceding discussion and the discussion presented in Sec. II, temperature is the basic parameter that determines the ice crystal size distribution and the position of the cloud via the threshold RH. Once the size distribution is known, the single-scattering properties may be calculated. Moreover, having the position of cirrus clouds in the atmosphere and the geometry governing the detector–target system defined, radiative transfer calculations may be carried out.

As shown, the ice crystal size distribution is dependent on the temperature in clouds. To simplify radiative transfer calculations, we may perform an averaging procedure over the single-scattering parameters to account for the inhomogeneity of the size distribution.

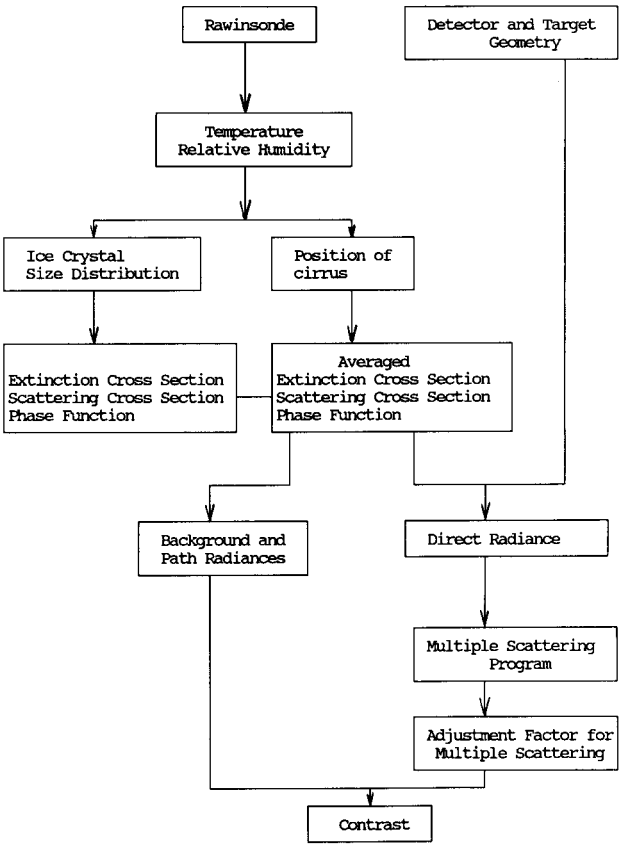

Fig. 3. Block diagram for the IR transmission model for cirrus cloud developed in the present study.

For example, the averaged extinction coefficient may be computed from

$$\bar{\beta}_e = \frac{1}{(z_t - z_b)}\int_{z_b}^{z_t} \beta_e[\lambda, T(z)]dz, \quad (52)$$

where z_b and z_t denote the cloud base and top heights, respectively. Once the averaged single-scattering parameters are known, the direct radiance, radiances produced by multiple scattering of cloud particles, background radiance, and path radiance can be computed from the radiative transfer program described in Sec. III. Using these radiances, the contrast for a target–detector system may be computed to investigate the relative importance of the presence of cirrus clouds in the transmission of infrared radiation. A block diagram that describes the aforementioned computational programs is displayed in Fig. 3.

The present IR radiative transfer program includes the contribution due to water vapor absorption. The absorption coefficients for water vapor in the window regions were taken from values available in LOWTRAN5.[11] The effects of water vapor absorption can be incorporated into the transfer program by adjusting the optical depth and single-scattering albedo.

The program was used to compute the direct radiance, path radiance, and background radiance associated with a target–detector system. We have selected two IR wavelengths of 3.7- and 10-μm, along with a midlatitude winter atmosphere in the radiance simula-

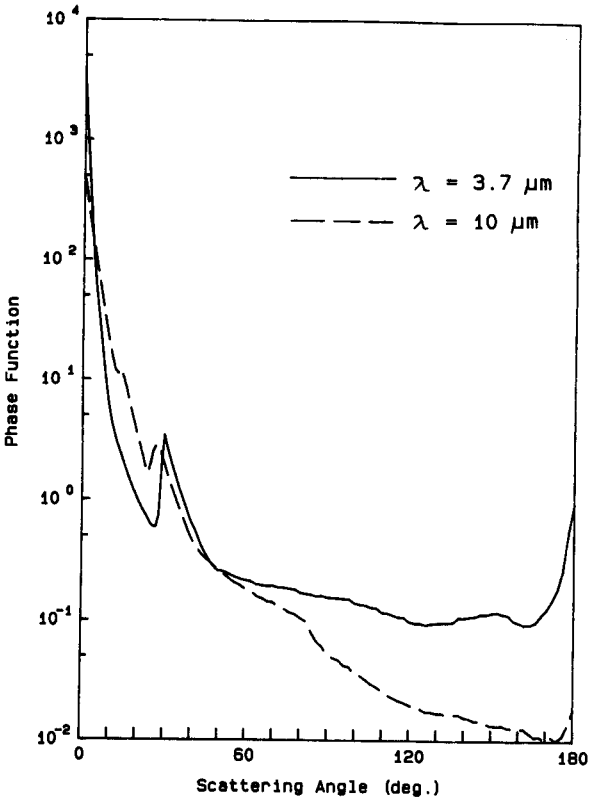

Fig. 4. Scattering phase functions for randomly oriented hexagonal ice crystals at the wavelengths of 3.7 and 10 μm. The ice crystal size distribution used in the calculations corresponds to a temperature of −40°C.

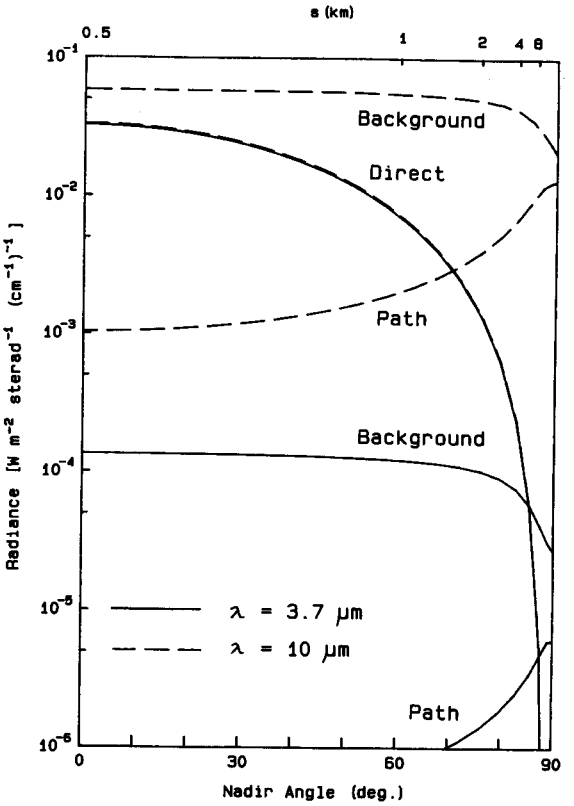

Fig. 5. Background, path, and direct radiances as functions of the nadir angle θ at the cirrus cloud top for a model midlatitude winter atmosphere. The upper scale is the path length defined as $s = \Delta z/\cos\theta$, where Δz is the cloud thickness.

tion. In addition, the following parameters were used: target equivalent radius r_t = 1 m, target equivalent temperature T_t = 873.2 K, half beamwidth of the detector ψ = 1°, cloud top height z_t = 8.5 km, and cloud base height z_b = 8 km. We used six temperatures corresponding to each 100 m to get the ice crystal size distributions. Using the parameterization equations developed in Sec. II and Eq (52), the optical depths and single-scattering albedos computed for the 3.7-μm wavelength are 0.1156 and 0.7144, respectively. For the 10-μm wavelength, they are 0.1155 and 0.6119. Strictly speaking, the phase function is also dependent on temperature. Using temperatures of −20, −40, and −60°C, we find that the computed phase functions deviate only insignificantly. As far as the radiative transfer calculations are concerned, these deviations can be neglected. Figure 4 shows the phase functions for randomly oriented ice crystals at 3.7- and 10-μm wavelengths using a temperature of −40°C. For the 3.7-μm wavelength, the distinct maximum located at the scattering angle of ~30° is the halo feature. Also, the backscattered energy is much larger than that for the 10-μm wavelength.

Figure 5 shows the computed radiances for 3.7- and 10-μm wavelengths as functions of the nadir angle θ or the path length $s = (z_t - z_b)/\cos\theta$. Because of the small water vapor concentration in the winter atmosphere, the computed background radiances for nadir angles less than ~60° are close to the emitted radiance from the surface with a temperature of 272.2 K. The background radiance at 3.7 μm is 3 orders of magnitude smaller than that at 10 μm. The direct radiance is inversely proportional to the square of the path length s. Its values decrease significantly as s (or θ) increases. The target equivalent temperature used in the calculation is 873.2 K. Because of this high temperature, the direct radiances at 3.7- and 10-μm wavelengths are almost identical. For the path radiance, the limb brightening effects are evident for nadir angles close to 90°. At the 3.7-μm wavelength the path radiance is extremely small.

Next, the significance of multiple scattering is investigated. Figure 6 illustrates the ratios of the first-order and second-order scattered radiances to the direct radiance. At the 10-μm wavelength, the contribution due to first-order scattering is generally <1%, except for nadir angles larger than ~80°. The first-order scattering contribution at the 3.7-μm wavelength accounts for more than ~2%. For large nadir angles, this contribution is significant. The second-order scattering contribution is ~2 orders of magnitude smaller than the first-order scattering at both wavelengths. For all practical purposes, the effects of multiple scattering due to cloud particles may be neglected if the half beamwidth of the detector is <1°. As shown in Fig. 6, the scattered radiances at 3.7 μm

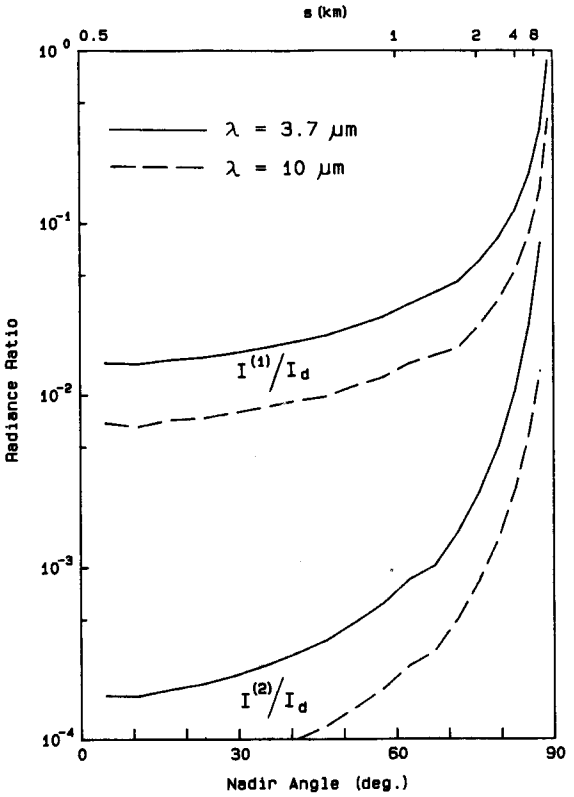

Fig. 6. Ratios of scattered radiances to the direct radiance, $I^{(1)}/I_d$ and $I^{(2)}/I_d$ as functions of the nadir angle or path length.

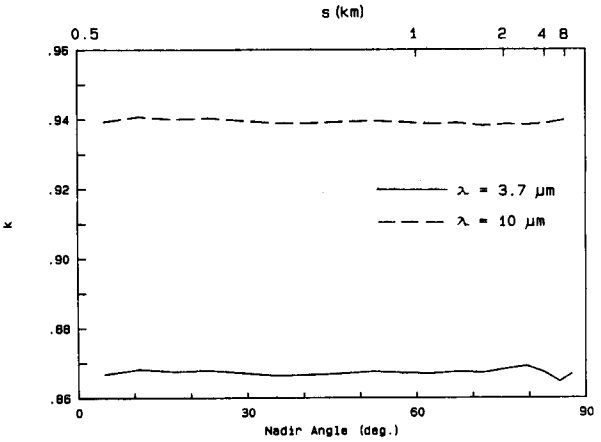

Fig. 7. Multiple scattering adjustment factor k defined in Eq. (46) as a function of the nadir angle or path length.

are larger than those at 10 μm. This is because the single scattering albedo and the Fraunhofer diffraction peak are larger for the former wavelength.

Figure 7 shows the adjustment k defined in Eq. (46). Because of larger scattering contributions at the 3.7-μm wavelength, k is smaller. This factor is largely independent of the nadir angle for both 3.7- and 10-μm wavelengths. If scattering effects higher than first-order are neglected, a simplified expression may be derived for the adjustment factor k. On the basis of Eqs. (17), (24) and (44), we find

Table I. Multiple Scattering Adjustment Factor k

$\lambda(\mu m)/\psi(°)$	0.5	1.0	1.5
3.7	0.921	0.867	0.831
10	0.970	0.941	0.916

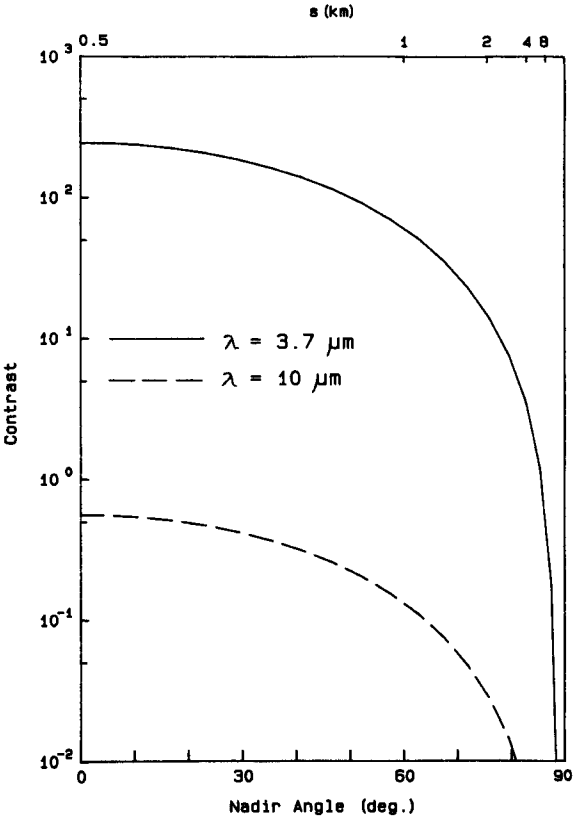

Fig. 8. Contrast as a function of the nadir angle or path length for 3.7- and 10-μm wavelengths. The parameters used in the calculations are as follows: target equivalent radius r_t = 1 m, target equivalent temperature T_t = 873.2 K, half beamwidth of the detector ψ = 1°, cloud base height z_b = 8 km, and cloud thickness Δz = 0.5 km.

$$k(\lambda,\psi) \cong 1 - \frac{\tilde{\omega}(\lambda)}{2}\int_0^{\bar{\psi}} P(\Theta)\sin\Theta d\Theta, \tag{53}$$

where

$$\bar{\psi} = \begin{cases} 1.621\psi + 0.558 & \text{for } \lambda = 3.7\ \mu m \\ 2.089\psi + 0.895 & \text{for } \lambda = 10\ \mu m. \end{cases} \tag{54}$$

In Table I, the values of k are listed for a number of values of ψ and two wavelengths.

The contrast in the presence of cirrus clouds as a function of the nadir angle is shown in Fig. 8. The contrast decreases as the nadir angle increases. At the 3.7-μm wavelength, the background and path radiances are much smaller than the direct radiance, as illustrated in Fig. 5. For this reason, the contrast is remarkably high. However, a low contrast in the case of 10μm is shown due to large background radiance.

Finally, we investigate the sensitivity of the contrast at λ = 3.7 μm to various pertinent parameters, includ-

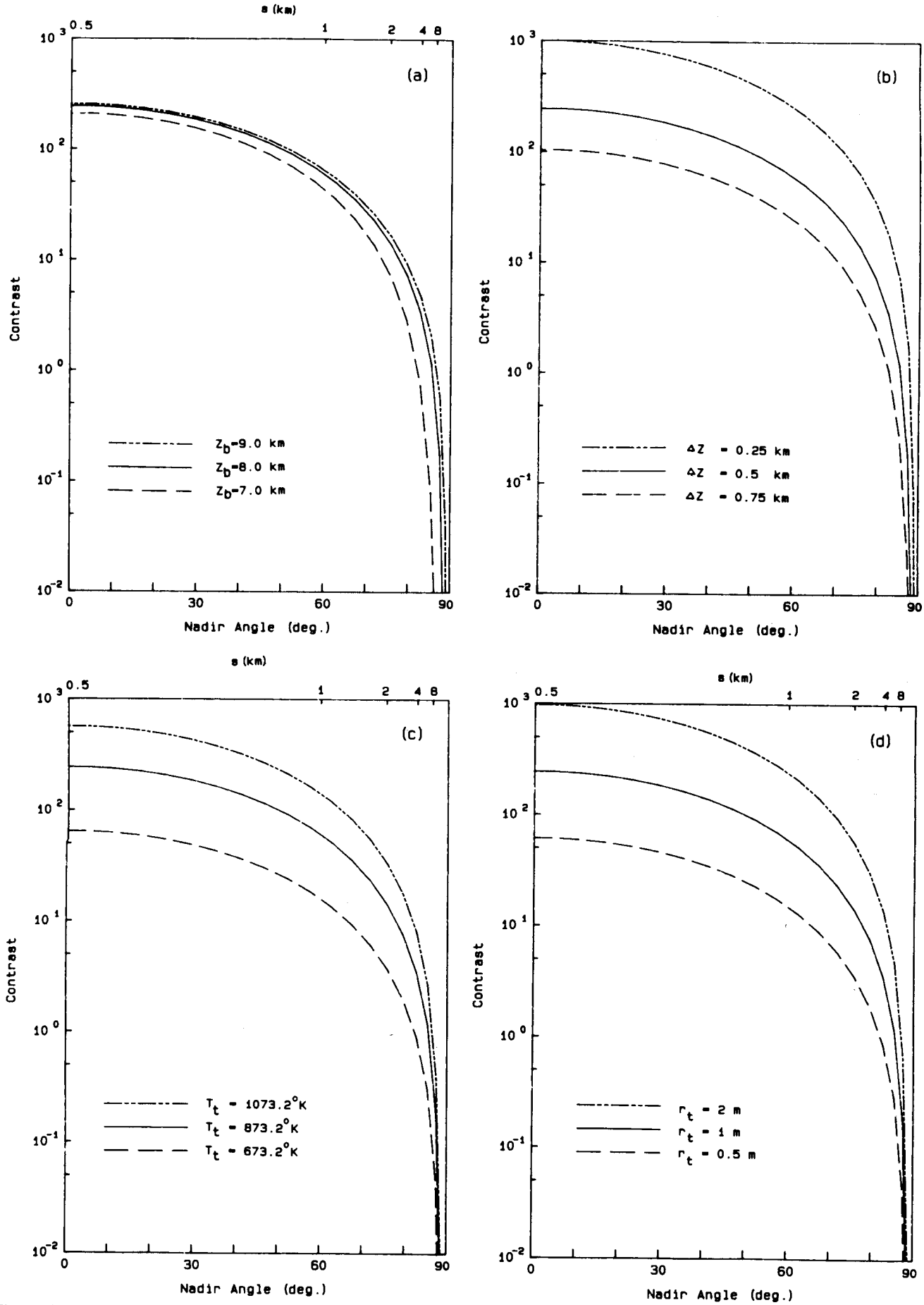

Fig. 9. Sensitivity of the contrast at $\lambda = 3.7\ \mu$m to (a) the cloud base height (7, 8, and 9 km), (b) the cloud thickness (0.25, 0.5, and 0.75 km), (c) the target equivalent temperature (1073.2, 873.2, and 673.2 K), and (d) the equivalent radius (2, 1, and 0.5 m). See the text for the parameters used in each case.

ing the cloud base height, cloud thickness, target temperature, and target radius. Figure 9(a) shows the contrast as a function of the nadir angle (or path length) for three cloud base heights of 7, 8, and 9 km. The cloud thickness Δz is fixed at 0.5 km and other parameters are the same as before unless otherwise stated in the discussion. As presented in Sec. II, the ice crystal size distribution is dependent on temperature, which is a function of height. Warmer temperatures would produce larger ice crystals and larger IWC. The optical depth is directly proportional to the ice water path ($= \Delta z \cdot \text{IWC}$). As a result, the optical depth increases as the cloud is lowered, as shown in Table II. A factor of ~10 in the optical depth is shown when the mean cloud temperature varies by 12 K (from 7 to 9 km). Since larger ice crystals absorb more radiation than small ice crystals, the single-scattering albedo decreases as temperature increases. Although its values vary by only ~0.1, this variation could have significant effects on the long path transmission. The contrasts presented in Fig. 9(a) are a result of competition between the optical depth and single-scattering albedo. For the case involving the cloud bases of 8 and 9 km, contrast results do not vary significantly. However, in the case of the 7-km cloud base, noticeable reductions of the contrast occur for larger nadir angles or longer path lengths ($s > 3$ km).

In recent years, there have been suggestions that some cirrus clouds may contain substantial numbers of ice crystals <20 μm that are not been detected by imaging probes. These suggestions have been made on the basis of indirect radiometer, satellite, and lidar observations during the First ISCCP (International Satellite Cloud Climatology Program) Regional Experiment (FIRE), which was carried out in Wisconsin, Oct.–Nov., 1987. Although the direct evidence of small ice crystals <20 μm in cirrus clouds has not been available at this point, their presence may have significant effects on the transfer of some of the IR wavelengths. We have performed additional experiments that include smaller ice crystals (10–20 μm) in light scattering and absorption calculations by extrapolation of the size distribution in the logarithmic scale presented in Eq. (1). For the case involving the 8–8.5 km cloud, the optical depth and single-scattering albedo are 0.1521 and 0.7650, respectively. However, contrast results are practically the same as those computed without small ice crystals.

Figure 9(b) is an illustration of the effect of the cloud thickness on the contrast. As shown in Fig. 5, the background radiance is small for the 3.7-μm wavelength. Thus the contrast is primarily produced by the scattered radiance due to the cloud and path radiance defined in Eqs. (44) and (48). Both radiances depend on the geometric factor, $(r_t/s\psi)^2$, that relates the target and detector field-of-views. The path length s is given by $\Delta z/\cos\theta$. Thus the total radiance is inversely proportional to Δz^2. This explains why the contrast is greatly reduced for larger thicknesses. On the basis of the results presented in Figs. 9(a) and (b), we conclude that the effect of optical depth of thin cirrus on the contrast at the 3.7-μm wavelength is relatively small.

In Fig. 9(c) we present the effect of the target temperature on the contrast. From Eq. (44), the direct radiance and radiances due to multiple scattering are directly proportional to the Planck function, which increases as temperature increases. As pointed out previously, because of the low background radiance at 3.7-μm, the contrast at this wavelength is linearly related to the geometric factor, $(r_t/s\psi)^2$. The results presented in Figs. 9(a)–(c) may be applied to a hot target located at the ground, such as an initial stage of forest fire. Let the half beamwidth ψ be fixed at 1°. The hot target at the ground would have a path length $s' = (z_b + \Delta z)/\cos\theta$ that differs from $s = \Delta z/\cos\theta$, corresponding to the case when the target is just below the cloud. It follows that to have the same geometric factor, we must have $r_t' = r_t(z_b + \Delta z)/\Delta z$. If $r_t = 1$ m, $z_b = 8$ km, and $\Delta z = 0.5$ km, $r_t' = 17$ m. There appears to be sufficient contrast for the detection of a ground fire using the 3.7-μm channel even when thin cirrus are present. Finally, the effect of the target radius r_t on the contrast is shown in Fig. 9(d). Since the total radiance is directly proportional to r_t^2, the results presented in this figure are self explanatory.

Table II. Single-Scattering Properties of Cirrus Clouds Corresponding to the Results Presented in Fig. 9(a).

z_t (km)	z_b (km)	T (K)	τ	$\tilde{\omega}$
9	9.5	224.2	0.0440	0.7607
8	8.5	230.2	0.1156	0.7144
7	7.5	236.2	0.3942	0.6803

V. Conclusions

An IR transmission model involving thin cirrus clouds has been developed for a target–detector system. On the basis of the successive order-of-scattering approach, the effects of multiple scattering of ice crystals within the detector field-of-view can be properly accounted for in the model. Although the theoretical formulations were for thermal IR emission, they may be modified to include the contribution due to the reflection of solar radiation. To simplify the multiple scattering contribution in the model, an adjustment factor in the exponential direct transmission term has been derived. This factor is expressed in terms of the half beamwidth of the detector and wavelength.

In connection with scattering and absorption calculations, we have presented parameterization expressions for the ice crystal size distribution in terms of temperature based on cloud physics data derived by Heymsfield and Platt.[2] To facilitate scattering and absorption computations, the single-scattering properties, including the extinction cross section and single-scattering albedo for randomly oriented columns and plates are parameterized in terms of the maximum dimension of ice crystals and wavelength. We have also developed a simple relative humidity technique for the prediction of cirrus cloud height. The thresh-

old relative humidity above which cirrus clouds are allowed to form in the atmosphere is determined as a function of temperature. However, this technique requires further verification.

Using the present IR transmission model along with the single-scattering parameters computed from the observed ice crystal size distribution, the direct radiance, path radiance, radiances produced by multiple scattering of ice crystals, and background radiation have been computed for 3.7- and 10-μm wavelengths. The background and path radiances in the presence of cirrus clouds were computed from the adding method for multiple scattering developed by Takano and Liou.[9] For both wavelengths, contributions from scattering events higher than first-order scattering may be neglected due to substantial absorption by ice particles. We show that the background radiance at the 3.7-μm wavelength is relatively small so that a high contrast may be obtained using this wavelength for the detection of objects in the presence of thin cirrus clouds. Sensitivity of the contrast at this wavelength to the cloud height and thickness, and target temperature and radius has been examined. The most important parameters that determine the contrast are the target temperature and geometric factor $(r_t/s\psi)$ where r_t is the target radius, $s = \Delta z/\cos\theta$, Δz the cloud thickness, θ the zenith angle of the detector, and ψ the half beamwidth of the detector. Although the present formulations are primarily developed for application to the detection of airborne objects, they are equally applicable to the detection of hot ground sources, such as forest fires. This may be done by redefining the aforementioned geometric factor.

This research was supported, in part, by Horizons Technology, Inc., under the support of IASPM Subcontract 5728-88-002 and the Division of Atmospheric Sciences of the National Science Foundation under grant ATM-8815712.

References

1. K. N. Liou, "Influence of Cirrus Clouds on Weather and Climate Processes: A Global Perspective," Mon. Weather Rev. **114,** 1167–1199 (1986).
2. A. J. Heymsfield and C. M. R. Platt, "A Parameterization of the Particle Size Spectrum of Ice Clouds in Terms of the Ambient Temperature and the Ice Water Content," J. Atmos. Sci. **41,** 846–855 (1984).
3. Y. Takano and K. N. Liou, "Solar Radiative Transfer in Cirrus Clouds. Part I: Single-scattering and Optical Properties of Hexagonal Ice Crystals," J. Atmos. Sci. **46,** 3–19 (1989).
4. A. J. Heymsfield, "Cirrus Uncinus Generating Cells and the Evolution of Cirriform Clouds. Part I. Aircraft Observations of the Growth of the Ice Phase," J. Atmos. Sci. **32,** 799–808 (1975).
5. A. J. Heymsfield, "Precipitation Development in Stratiform Ice Clouds: A Microphysical and Dynamical Study," J. Atmos. Sci. **34,** 367–381 (1977).
6. S. Warren, "Optical Constants of Ice from the Ultraviolet to the Microwave," Appl. Opt. **23,** 1206–1225 (1984).
7. A. H Auer, Jr. and D. L. Veal, "The Dimension of Ice Crystals in Natural Clouds," J. Atmos. Sci. **27,** 919–926 (1970).
8. C. M. R. Platt and Harshvardhan, "Temperature Dependence of Cirrus Extinction: Implication for Climate Feedback," J. Geophys. Res. **93,** 11051–11058 (1988).
9. Y. Takano and K. N. Liou, "Solar Radiative Transfer in Cirrus Clouds. Part II: Theory and Computation of Multiple Scattering in an Anisotropic Medium," J. Atmos. Sci. **46,** 20–36 (1989).
10. R. W. Pratt, "Review of Radiosonde Humidity and Temperature Errors," J. Atmos. Ocean. Tech., **2,** 404–407 (1985).
11. F. J. Kneizys *et al.*, "Atmospheric Transmittance/Radiance: Computer Code LOWTRAN5," Scientific Report, AFGL-TR-80-0067, Air Force Geophysics Laboratory (1980).